The global patterns of instantaneous CO_2 forcing at the top-of-atmosphere and surface

Yan-Ting Chen,[a] Yi Huang,[a] and Timothy M. Merlis[b]

[a] *Department of Atmospheric and Oceanic Sciences, McGill University, Montreal, Quebec, Canada*
[b] *Program in Atmospheric and Oceanic Sciences, Princeton University, Princeton, NJ, USA*

ABSTRACT: The radiative forcing of carbon dioxide (CO_2) at the top-of-atmosphere (TOA) has a rich spatial structure and has implications for large-scale climate changes, such as poleward energy transport and tropical circulation change. Beyond the TOA, additional CO_2 increases downwelling longwave at the surface, and this change in flux is the surface CO_2 forcing. Here, we thoroughly evaluate the spatiotemporal variation of the instantaneous, longwave CO_2 radiative forcing at both the TOA and surface. The instantaneous forcing is calculated with a radiative transfer model using ERA5 reanalysis fields. Multivariate regression models show that the broadband forcing at the TOA and surface are well-predicted by local temperatures, humidity, and cloud radiative effects. The difference between the TOA and surface forcing, the atmospheric forcing, can be either positive or negative and is mostly controlled by the column water vapor, with little explicit dependence on the surface temperature. The role of local variables on the TOA forcing is also assessed by partitioning the change in radiative flux to the component emitted by the surface vs. that emitted by the atmosphere. In cold, dry regions, the surface and atmospheric contribution partially cancel out, leading to locally weak or even negative TOA forcing. In contrast, in the warm, moist regions, the surface and atmospheric components strengthen each other, resulting in overall larger TOA forcing. The relative contribution of surface and atmosphere to the TOA forcing depends on the optical thickness in the current climate, which, in turn, is controlled by the column water vapor.

1. Introduction

The radiative forcing of carbon dioxide (CO_2) at the top-of-atmosphere (TOA) plays a central role in quantifying climate change and its global-mean value is a key aspect of radiative feedback analysis. Beyond the global mean, it has been recognized that the TOA radiative forcing of CO_2 is spatially inhomogeneous because of its relation to local atmospheric conditions (e.g., Feldl and Roe 2013; Zhang and Huang 2014; Huang et al. 2016, 2017; Jeevanjee et al. 2021). Previous literature has shown that the forcing distribution associated with current climate can drive changes in the mean tropical circulation (Merlis 2015; Shaw and Tan 2018) and poleward energy transport (Huang et al. 2017), owing to the differential forcing that arises from the consequences of the climatological spatial structure of temperature, water vapor, and cloud distribution on the forcing. In addition to altering Earth's energy balance at TOA, CO_2 increases affect the downwelling longwave radiation at the surface (Collins et al. 2006; Feldman et al. 2015).

The difference between the TOA and surface forcing of CO_2 affects the *atmospheric* energy balance and this, in turn, constrains the hydrological cycle response on fast timescales when the surface warming is small (Allen and Ingram 2002; Pendergrass and Hartmann 2014; Samset et al. 2016) and is an important energetic consideration in solar radiation geoengineering schemes (Seeley et al. 2021). Moreover, the traditional TOA-centered perspective has the limitation in the context of energy transport because it affects the combined ocean and atmosphere transport, so the additional information from surface forcing can be used to isolate the atmospheric component of the change in energy transport (Huang et al. 2017). A thorough understanding of CO_2 radiative forcing at both the TOA and the surface is therefore critical to important aspects of both regional and global climate change.

There are two schools of thoughts as to what give rise to instantaneous forcing: saturation of absorption bands (Pierrehumbert 2010; Jeevanjee et al. 2021; Romps et al. 2022) and displacement of effective emission layer (Huang and Bani Shahabadi 2014; Dufresne et al. 2020). These two perspectives suggest distinct components of the atmosphere are critical to the forcing: the saturation of absorption bands focuses on the magnitude of emission temperature, while the emission-layer argument highlights the lapse rate around the emission height. Aside from different views of the relevant temperatures, the emission temperature itself results from underlying spectral variations, so that the quantitative connection between an atmospheric profile and the instantaneous forcing is challenging.

Recent work has attempted to analytically quantifying the instantaneous CO_2 forcing at the TOA, with simplifications to keep calculations manageable: wavelength-varying absorption spectrum and complications of water vapor have been omitted. For example, Jeevanjee et al. (2021) considered how the broadening of the absorption bandwidth blocks surface emission, allowing for a relationship between this change in bandwidth and the surface temperature that determines the TOA forcing in a dry atmo-

Corresponding author: Yan-Ting Chen, yanting.chen@mail.mcgill.ca

sphere. With moisture, however, the broadened CO_2 absorption blocks emission from water vapor instead, which is hard to estimate by simple approximations and results in a non-negligible bias in the forcing estimate in midlatitudes. In contrast, Dufresne et al. (2020) examined a realistic atmospheric profile and concluded that the emission layer displacement (a shift to higher elevations with increased CO_2) dominates the CO_2 forcing, and the amount of emission layer change is insensitive to water vapor amount. Yet, a pre-requisite of emission layer displacement argument to hold is that the absorptivity is saturated and it is, therefore, not applicable in the atmospheric window (Huang and Bani Shahabadi 2014; Dufresne et al. 2020). The broadband bias would be even larger in the dry regions, where a considerable amount of outgoing longwave flux stems from the surface via the atmospheric window (e.g., Costa and Shine 2012).

Compared with the TOA forcing, CO_2 forcing at the surface has been less thoroughly investigated. Conceptually, one might expect the surface forcing follows a similar line of thought as the TOA forcing with competing perspectives on absorption change and emission layer displacement. However, there are difficulties that arise because the effective emission layer for downward flux is intertwined with absorption change. This stands in contrast to the upward flux at the TOA, where these two terms can be roughly separated and the effective emission can be approximated as the layer where the optical depth is unity (though the exact number depends on the choice of vertical coordinate, Jeevanjee and Fueglistaler 2020). At the surface, the majority of downward flux comes from very bottom of the atmosphere with decaying contribution from air above. In response to changes in CO_2 concentration, the e-folding length of the decaying contribution changes and this is sensitive to the detailed near-surface atmospheric structure. Freese and Cronin (2021) considered the broadening of absorption band, which only depends on CO_2 concentration, along with surface temperature to estimate the Antarctic surface forcing. This implicitly assumes a fixed effective emission layer. But we will later show that this method cannot explain the local minimum of surface forcing in the deep tropics, where the surface temperature can be locally warmer. An alternative approach is to lump all variables into an effective emission height, but it has been reported to fail in moist regions (Shakespeare and Roderick 2021).

Collectively, the current physical understanding of CO_2 forcing suggests it is a challenge to formulate a quantitatively accurate forcing estimates that can capture the range of climate states observed on Earth. This leaves semi-empirical perspectives, such as the multivariate regression model in Huang et al. (2016) that use convenient atmospheric variables to predict CO_2 forcing, as a valuable and practical approach to characterize and quantify the forcing's structure.

In this study, we provide an in-depth examination of CO_2 forcing pattern at the TOA, surface, and atmosphere, including their annual-mean pattern, seasonal cycle, and the controlling factors. We also quantify the relative contribution of the surface emission vs. atmospheric contributions to the TOA forcing to shed light on the roles of absorption band saturation and emission layer changes. The paper will proceed as follows. Section 2 describes the radiative transfer model and dataset we use. In section 3, we document the complete instantaneous CO_2 forcing pattern and its temporal variability. Then, the multivariate regression models are used to identify the controlling factors of CO_2 forcing (section 4), furthering Huang et al. (2016) to the surface and atmospheric forcing for a more comprehensive understanding. In section 5, we scrutinize the cause of TOA forcing from a spectroscopic perspective, which provides a new perspective on the relationship between CO_2 forcing at the TOA, surface, and atmosphere. Last, conclusions and discussion are given in section 6.

2. Model and data

The radiative fluxes are calculated by a standalone Rapid Radiative Transfer Model, a version that has been widely used in general circulation models (RRTMG, Iacono et al. 2008). The longwave component of RRTMG, ranging from 10 cm^{-1} to 3250 cm^{-1}, computes the fluxes in 16 bands. The atmospheric data we use is taken from the hourly ERA5 reanalysis dataset of the European Centre for Medium-Range Weather Forecasts, while the skin temperature and surface pressure over land are replaced by the hourly ERA5-land dataset. The well-mixed greenhouse gas concentrations of CO_2, CH_4, and N_2O are prescribed to 380, 1.797, and 0.323 ppmv, respectively as in Huang et al. (2016). The calculations are repeated with doubled CO_2 concentration (760 ppmv), with all other variables are unchanged, and the instantaneous radiative forcing is defined as the difference between these two computed fluxes. We focus on the longwave component of forcing, as the CO_2 forcing associated with the shortwave is rather homogeneous (Huang et al. 2016). The radiation fluxes are calculated with $2.5°\times 2.5°$ horizontal resolution for every hour over the 19 years period 2000–2018.

3. The forcing pattern and variation

a. Spatial variation: Climatology

The 19-year average of instantaneous CO_2 forcing pattern is shown in Figure 1. Under clear-sky, the global-mean forcing is $2.83\,W\,m^{-2}$ at the TOA and $2.42\,W\,m^{-2}$ at the surface, resulting in a convergence of $0.41\,W\,m^{-2}$ within the atmosphere: this difference defines the atmospheric forcing. The forcing evolves with the base climate during the course of 19 years. From 2000 to 2018, the annual-mean TOA forcing varies between 2.80 and $2.86\,W\,m^{-2}$

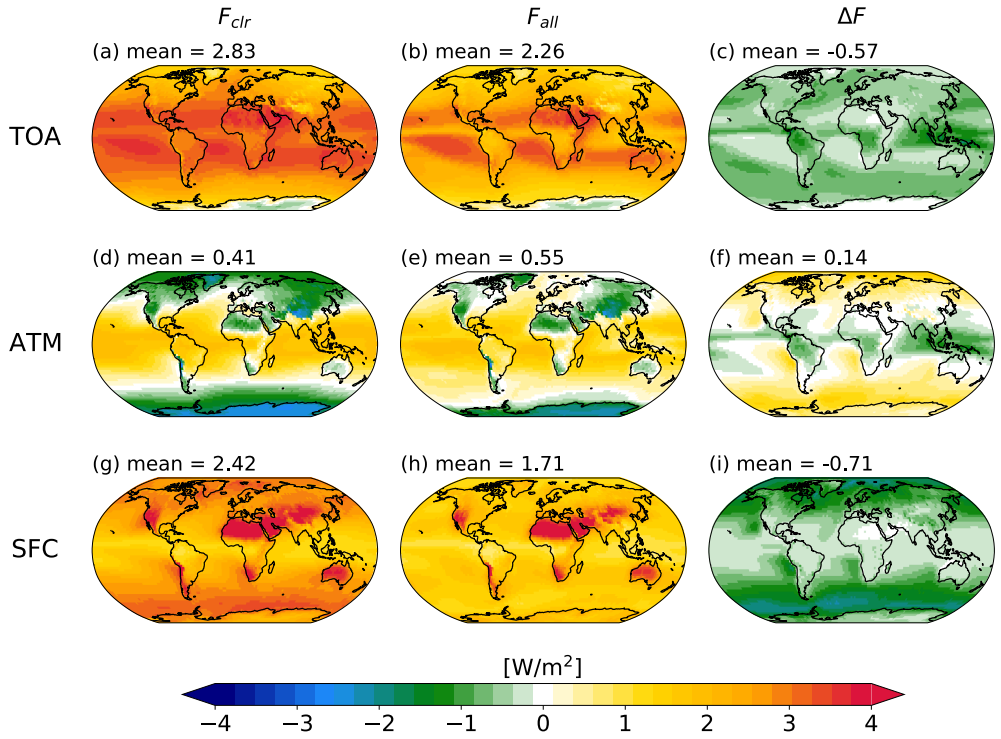

FIG. 1. The instantaneous radiative of forcing 2× CO_2 (in $\mathrm{W\,m^{-2}}$). From top to bottom row: the forcing at the TOA, in the atmosphere, and at the surface. From left to right column: the forcing under clear-sky (F_{clr}), all-sky (F_{all}), and the cloud masking effect (ΔF) on the forcing.

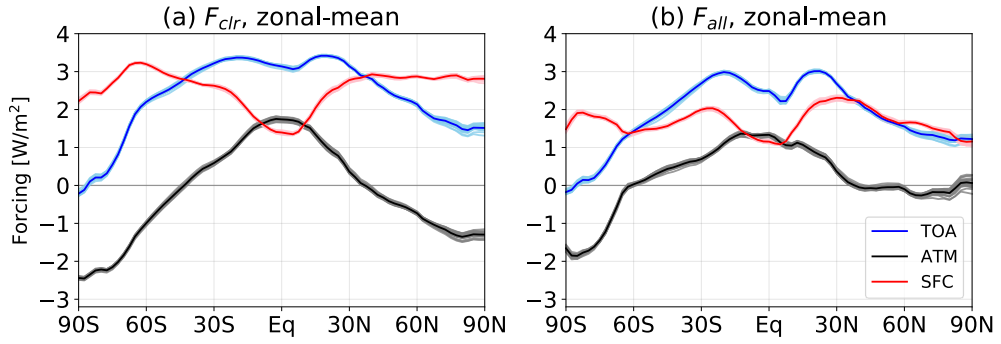

FIG. 2. The zonal-mean of annual-mean instantaneous forcing. The thickened line denotes the 19-year climatology, with the annual mean of individual years plotted in a lighter color.

and the surface forcing varies between 2.44 to 2.40 $\mathrm{W\,m^{-2}}$, with no clear trend during the period. The TOA and surface forcing do not always co-vary, so the magnitude of the atmospheric forcing fluctuates between 0.36 $\mathrm{W\,m^{-2}}$ in 2000 to 0.46 $\mathrm{W\,m^{-2}}$ in 2018. The clouds decrease the global-mean TOA and surface forcing by 0.57 and 0.71 $\mathrm{W\,m^{-2}}$, respectively, and they result in an increase of the all-sky atmospheric forcing by 0.14 $\mathrm{W\,m^{-2}}$. Compared with Pincus et al. (2020), who sampled a subset of reanalysis profiles with line-by-line radiative transfer calculations, the magnitude of clear-sky, global-mean TOA forcing is similar to documented 2.71 $\mathrm{W\,m^{-2}}$ in their study, yet the surface forcing we report here is 20% larger than their results. Another similar calculation is Huang et al. (2017), who calculated an all-sky forcing based on a global climate model's atmospheric state of 2.6 $\mathrm{W\,m^{-2}}$ at the TOA and 1.4 $\mathrm{W\,m^{-2}}$ at the surface, meaning a difference of around 15% at the TOA and 30% at the surface. Although these numbers are not be directly comparable as a results of several factors, such as difference on the choice of base climate, initial CO_2 concentration, sampling location and radiative transfer model used, these results together provide an indication of the variability in the range of forcing values.

Figure 1 shows that the forcing pattern displays a first-order dependence on latitude, especially for the clear-sky (F_{clr}, left column). The clear-sky TOA forcing decreases from the low to high latitudes, ranging from 3.4 to 1.5 $\mathrm{W\,m^{-2}}$ with a weak but discernible local minimum in the deep tropics, where the forcing slightly decreases to 3 $\mathrm{W\,m^{-2}}$. This relatively small forcing in the moist region has been identified as the water vapor masking effect (Huang et al. 2016; Jeevanjee et al. 2021), because the absorption by extra CO_2, which centers around 15μm, is blocked by the rotation band of pre-existing water vapor. The forcing in polar regions is strongly hemispheric asymmetric and is negative in the Antarctic, consistent with previous work (Zhang and Huang 2014; Schmithüsen et al. 2015; Huang et al. 2016). The clear-sky surface forcing exhibits a local minimum in the tropics like the TOA component but is more prominent, owing to the stronger water vapor masking effect. Additionally, the surface forcing is more zonally asymmetric, with amplified forcing over dry regions and mountains (the Sahara Desert, Australian deserts, the Rockies, and the Andes) that exceeds 4 $\mathrm{W\,m^{-2}}$ in the annual mean. The resulting atmospheric forcing enhances the equator-to-pole energy gradient due to it being positive at the equator and decreasing poleward. We also note that in dry regions, the strong surface forcing exceeds the TOA forcing and creates zonally anomalous negative atmospheric forcing.

The all-sky forcing (F_{all}) and the difference between the all-sky and clear-sky, the cloud masking effect (ΔF), are shown in Figure 1 (middle and right columns). Clouds strongly modulate the TOA and surface forcing. The all-sky TOA forcing shows a clear trace of the tropical rain belt with locally small forcing, suggesting a stronger masking effect by water vapor and clouds combined. The clouds also reduce forcing in the extratropics by 0.6 $\mathrm{W\,m^{-2}}$. In contrast to the TOA forcing, the dominant feature of the all-sky surface part is the exceptionally large forcing in the deserts and major mountain ranges where clouds rarely present. The latitudinal forcing dependence is largely eliminated by low clouds in the extratropics. In all-sky atmospheric forcing, one can also see that the clouds impose a non-negligible masking effect that smooth the meridional forcing gradient, with a reduced forcing peak around the equator and an overall increased forcing in the extratropics due to the surface forcing decrease. The strong negative clear-sky atmospheric forcing in the Arctic is also largely counteracted by clouds, bringing the annual-mean forcing close to neutral there.

Figure 2 shows the zonal-means of the annual-mean radiative forcing maps of Figure 1, with interannual variations shown in shading. For both clear-sky and all-sky, the surface forcing is relatively symmetric between the hemispheres. The TOA component has strong hemispheric asymmetry in the polar regions, with the forcing in the Arctic larger than in the Antarctica by 1 $\mathrm{W\,m^{-2}}$. Under clear-sky, although the local minimum of both the TOA and the surface forcing are located a bit northward of the equator, the atmospheric forcing peaks exactly at the equator. With clouds, the atmospheric forcing in the Northern Hemisphere is greatly enhanced in the polar region and does not monotonically decrease poleward anymore; it becomes rather close to zero between 35°N to 90°N, primarily due to reduced surface forcing in the higher latitudes. Additionally, the latitude that the atmospheric forcing flips sign in the Southern Hemisphere shifts poleward from 45°S for clear-sky to 60°S for all-sky conditions. The clouds also exert notable changes in the low latitudes, especially for the tropical TOA forcing. Within the tropics, the clouds lower the TOA forcing more than the SFC forcing and further mitigates the meridional forcing variation, with a greater forcing decrease around 5°N for the TOA and consequently smaller atmospheric forcing. With an outstanding local minimum of annual-mean TOA forcing that sits near 5° (consistent with the annual-mean ITCZ and associated clouds being north of the equator), the atmospheric forcing no longer peaks at the equator, and it instead has a broad local maximum between 0°S to 15°S. The inter-annual variability of the zonal- and annual-mean forcing is weak (shading in Fig. 2). The largest variability is in the Arctic, where the all-sky atmospheric forcing oscillates about zero with a range of 0.5 $\mathrm{W\,m^{-2}}$.

b. Seasonal variation

The instantaneous forcing also exhibits remarkable seasonality, as displayed in Figure 3. The forcing of each term, particularly in low latitudes, shows similar seasonal dependence in both hemispheres. For instance, the TOA and surface forcing in the subtropics are amplified in the wintertime and the local minimum migrates with the ITCZ, resulting in a weak movement of atmospheric forcing peak. The latitudinal extent of positive atmospheric forcing, however, does not simply synchronize with the tropical rain belt movement, especially when the cloud effect is considered. For example, the northernmost latitude that the atmospheric forcing changes sign falls in August, late boreal summer for clear-sky, and under all-sky the positive forcing blob can extend to the Arctic in boreal fall (August to November). In comparison, the southernmost latitude with positive atmospheric forcing occurs in June, the austral winter, for both clear and all-sky.

The polar region shows even more hemispheric asymmetry for the TOA and the atmospheric components. In particular, the TOA forcing in the Antarctic is negative from October to February, while it is always positive in the Arctic. The surface forcing is consistently positive and varies in a contrasting tendency to the TOA counterpart which further intensifies the atmospheric forcing variation. The seasonality of global-mean TOA and surface forcing (Fig. 3d,h) is opposite as well: the TOA forcing maximum

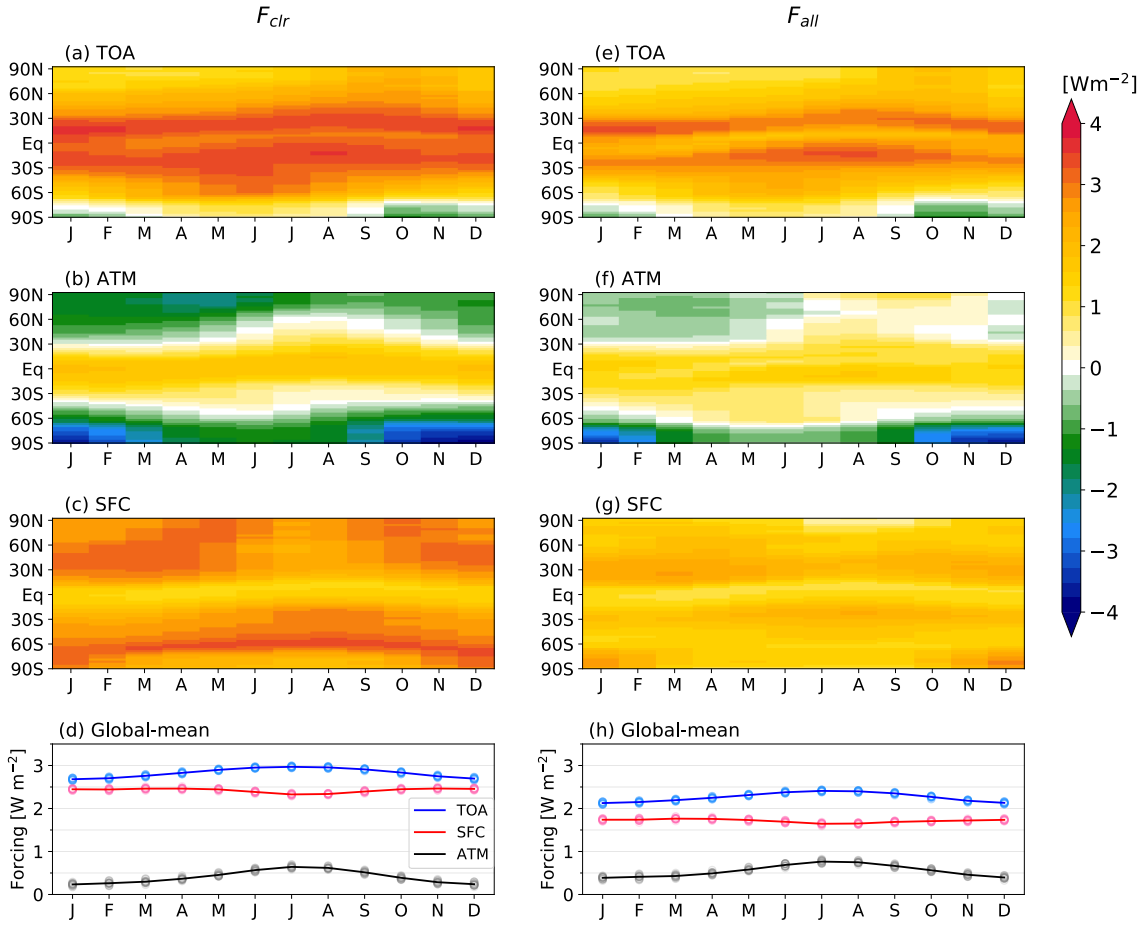

FIG. 3. The seasonality of climatological monthly average of zonal-mean clear-sky radiative forcing at the (a) TOA, (b) atmosphere, and (c) surface and the all-sky radiative forcing at the (e) TOA, (f) atmosphere, and (g) surface. The seasonality of global-mean forcing for clear-sky and all-sky are shown in (d) and (h), respectively. In panel (d) and (h), with each circle showing the global-mean of monthly-mean forcing in different years for the forcing at the (blue) TOA, (black) atmosphere, and (red) surface, with the 19-years averaged forcing connected in lines.

falls in July, which is exactly the time with surface forcing minimum. The all-sky forcing has similar seasonality as the clear-sky forcing, implying that change in forcing from cloud masking ΔF is rather constant temporally in the global average. In the next section, we will show that the seasonality of forcing is highly pertinent to the climatology of humidity and surface temperature, whose global-mean are greatest in July.

4. Regression model

In the previous section, we showed that the TOA, surface, and atmospheric forcing from a uniform doubling of the CO_2 concentration are highly inhomogeneous spatially and temporally. To further understand the dependence of the forcing pattern on the atmospheric and surface state, we begin from a statistical perspective following the multivariate regression analyses in Huang et al. (2016). In particular, we extend the regression model to the surface forcing. An expression for the atmospheric forcing can then be formed by calculating the by linear combination of the TOA and surface regression models. In this way, the CO_2 radiative forcing can be estimated directly from the local distributions of geophysical variables. This method also quantifies the sensitivity of the radiative forcing to variables.

The form of multivariate regression model is:

$$\hat{F} = F_0 + \sum_{i=0}^{n} A_i \frac{y_i - y_{i0}}{y_{i0}}, \tag{1}$$

where $\hat{F}$ is the forcing prediction, and the subscript 0 denotes the multiyear global average. The regression coefficients A_i are determined by the area-weighted least-squares regression method. The variables y_i are chosen geophysical variables that serve as predictors normalized by its global mean y_{i0}. This regression model, therefore, accounts for the spatial and temporal variations about the global mean, which is specified.

The central question is then, how to choose predictors that are physically meaningful and easily accessible? Huang et al. (2016) identified several key variables that well predict the clear-sky TOA forcing, including the surface temperature (T_s), stratospheric temperature at 10 hPa (T_{10}), and column water vapor (CWV, in $\mathrm{kg\,m^{-2}}$). The all-sky forcing is obtained by adding the cloud effect, which is predicted by the cloud radiative effect (CRE, in $\mathrm{W\,m^{-2}}$) in the current climate (Zhang and Huang 2014; Huang et al. 2016). To be specific, T_s captures the equator-to-pole thermal emission pattern that explains a large portion of forcing gradient. T_{10} identifies the surface–stratosphere temperature contrast, which is pertinent to the emission layer elevation within the stratosphere especially for the CO_2 absorption band (Huang et al. 2016; Jeevanjee et al. 2021; Romps et al. 2022). The water vapor usually damps the forcing by reducing the energy that additional CO_2 can absorb because the rotation band of H_2O molecules partially overlaps with CO_2 absorption in the far-infrared (referred to as water vapor masking of the CO_2 forcing). A similar argument holds for the cloud effect on the CO_2 forcing, which exhibits a wider absorption spectrum that is highly correlated to the current cloud radiative effect.

Narrowing the choice of predictors to those that are commonly available in the reanalysis and climate model output, we find that the square of column water vapor (CWV^2) is essential to predict the surface forcing well, on top of those variables that are already identified for the TOA forcing. The adoption of CWV^2 accounts for the pronounced water vapor absorption, such as the continuum absorption that is proportional to the square of concentration (Pierrehumbert 2010). The resulting regression models for clear-sky forcing $\hat{F}_{clr}$ are:

$$\begin{aligned}\hat{F}_{clr,TOA} = 2.83 &+ 15.85\,\frac{T_s - 288.4}{288.4} - 8.85\,\frac{T_{10} - 228.6}{228.6} \\ &+ 0.47\,\frac{\mathrm{CWV} - 24.4}{24.4} - 0.43\,\frac{\mathrm{CWV}^2 - 846.2}{846.2}\end{aligned} \tag{2}$$

$$\begin{aligned}\hat{F}_{clr,SFC} = 2.42 &+ 16.24\,\frac{T_s - 288.4}{288.4} + 0.55\,\frac{T_{10} - 228.6}{228.6} \\ &- 4.34\,\frac{\mathrm{CWV} - 24.4}{24.4} + 1.34\,\frac{\mathrm{CWV}^2 - 846.2}{846.2}\end{aligned} \tag{3}$$

for the TOA and surface forcing, with 98% and 91% variance explained, respectively. The atmospheric forcing is obtained by differencing the TOA and surface forcing:

$$\begin{aligned}\hat{F}_{clr,ATM} &= \hat{F}_{clr,TOA} - \hat{F}_{clr,SFC} \\ &= 0.41 - 0.39\,\frac{T_s - 288.4}{288.4} - 9.40\,\frac{T_{10} - 228.6}{228.6} \\ &\quad + 4.81\,\frac{\mathrm{CWV} - 24.4}{24.4} - 1.77\,\frac{\mathrm{CWV}^2 - 846.2}{846.2}.\end{aligned} \tag{4}$$

Although the predicting equations here include four variables for each, the TOA and surface forcing are well predicted by three predictors: T_s, T_{10}, and CWV for the TOA forcing, and T_s, CWV, and CWV^2 for the surface forcing. The fourth predictor is introduced to allow the atmospheric forcing to result from the difference of the TOA and SFC regression models. As the downward flux at the surface mainly stems from the emission in the lower troposphere with high water vapor concentrations, it is straightforward to expect a larger portion of forcing to be influenced by CWV at the surface than at the TOA. Similarly, the magnitude of the T_{10} coefficient in the surface forcing is less than 10% than that of the TOA forcing, suggesting a limited influence of stratospheric temperature at the surface.

The prediction for all-sky forcing is obtained by adding cloud masking effects on top of clear-sky equations:

$$\hat{F}_{all,TOA} = \hat{F}_{clr,TOA} + \widehat{\Delta F}_{TOA} \tag{5}$$

$$\hat{F}_{all,SFC} = \hat{F}_{clr,SFC} + \widehat{\Delta F}_{SFC} \tag{6}$$

$$\hat{F}_{all,ATM} = \hat{F}_{clr,ATM} + \widehat{\Delta F}_{ATM}, \tag{7}$$

where $\widehat{\Delta F}$ denotes the cloud masking effect, which is well-correlated to the cloud radiative effect (Zhang and Huang 2014). Using the cloud radiative effect at the TOA and the

surface as predictors, we get

$$\widehat{\Delta F}_{TOA} = -0.57 - 0.53\,\frac{\mathrm{CRE_{TOA}} - 20.06}{20.06} \tag{8}$$

$$\widehat{\Delta F}_{SFC} = -0.71 - 0.78\,\frac{\mathrm{CRE_{SFC}} - 21.84}{21.84} \tag{9}$$

$$\begin{aligned}\widehat{\Delta F}_{ATM} &= \hat{\Delta F}_{TOA} - \hat{\Delta F}_{SFC} \\ &= 0.14 - 0.53\,\frac{\mathrm{CRE_{TOA}} - 20.06}{20.06} \\ &\quad + 0.78\,\frac{\mathrm{CRE_{SFC}} - 21.84}{21.84}.\end{aligned} \tag{10}$$

Though simple in form, equations (8) and (9) explain more than 97% variance for the cloud masking effects.

As the regression models explain more than 90% of forcing variance, the map of predictors reveals each variable's role in the forcing variability since the predicted forcing pattern can be viewed as the superposition of predictor contributions. The climatology of normalized predictors is shown in Figure 4. The temperature predictors, T_s and T_{10}, vary mostly with latitude and have only slight zonal variation. This shows their role in explaining the meridional forcing gradient, consistent with the first-order dependence of the greenhouse effect on thermal emission. The strong zonal variation of CWV and CWV^2 in low latitudes accounts for the contrast between the dry, subsiding regions and moist, convecting regions within the tropics, a prominent aspect of the clear-sky surface forcing (Fig. 1). The cloud radiative effects at the TOA and surface reflect the high and low cloud cover, which are large magnitude in the tropical ascending region and midlatitudes respectively. This structure resembles the cloud effect on forcing, consistent with the CRE explaining more than 97% of the forcing variance.

The contribution of individual components in the regression models is further visualized in Figure 5 by combining the predictor patterns with coefficients in the regression models. For the TOA forcing, T_s is the dominant component, whereas T_{10}, CWV, and CRE all slightly offset it zonally and meridionally. The forcing dependence on temperature contrast between T_s and T_{10} can be viewed as a consequence of the "lapse rate" (Huang et al. 2016) or a "swap of surface and stratospheric emission" (Jeevanjee et al. 2021). The narrow belt with a local forcing minimum in the tropics is seen in CWV and CRE components, echoing the masking effect of water vapor and clouds (Merlis 2015; Huang et al. 2016). Interestingly, the negative forcing over the Antarctic seems well-captured by extremely cold T_s (Figs. 5a,m), without knowledge of near-surface temperature inversion that has been identified as a factor accounting for the negative greenhouse effect (Flanner et al. 2018). We find that T_s alone reproduces much of the forcing variation temporally because T_s dominates the surface–stratosphere temperature difference in most places. In Antarctica, however, T_{10} exhibits larger seasonal variation than T_s. The warmer T_{10} in southern hemisphere summer therefore contributes to negative TOA forcing from October to February [equation (2) and Fig. 3a].

For the surface forcing, the contribution by T_s is similar to the TOA prediction due to the similar magnitude of the regression coefficient, but the T_s component is offset by the substantial masking effect of CWV. CWV is a column-integrated quantity that is sensitive to the lower troposphere because of the bottom-heavy nature of specific humidity distribution, so one might intuitively expect a stronger CWV masking effect for surface forcing than the TOA. Of course, CWV may be closely related to T_s because the saturation specific humidity is governed by the Clausius–Clapeyron relation. However, the relative humidity can play an important role in shaping the zonal asymmetry of the forcing (Fig. 5i). Interestingly, unlike the TOA forcing where CWV and clouds show consistent signs of forcing anomaly in low latitudes, the pattern predicted by clouds is opposite to CWV because it is the low clouds rather than high clouds that are more relevant to the surface forcing (Figs. 4c,f). The cloud masking effect therefore more strongly occurs in the extratropics rather than the tropics for the surface forcing.

Although the atmospheric forcing is simply the forcing difference between two boundaries, some interesting results can be noted. First, the T_s contribution to the TOA and surface forcing almost cancel out, leaving this component even smaller than T_{10} [equation (4) and Figs. 5b,e]. Second, with strong CWV masking on the surface forcing, CWV is the dominant variable for the atmospheric forcing and accounts for the equator-to-pole forcing gradient (Fig. 5h). Moreover, as different cloud types exert distinct masking effects at the TOA and surface, the cloud masking effect does not simply cancel between the surface and TOA. Unlike the CWV masking which actually produces the meridional forcing gradient within the atmosphere, the clouds overall mitigate the atmospheric forcing contrast both zonally and meridionally (Fig. 5k).

The seasonality of predicted global-mean forcing is displayed in Figure 6. Overall, the picture of seasonality is in line with the results for the spatial pattern: the TOA forcing variation is best captured by T_s, the surface forcing is dominated by CWV seasonality while being opposite to T_s, and the atmospheric forcing is well represented by CWV. One new dimension is that, for temporal variability, T_{10} contributes more to TOA forcing than CWV and clouds. Also, the net cloud masking effect is quite steady among seasons. The largest bias in boreal summer can be traced back to larger underpredicted surface forcing in dry regions, including the Sahara Desert and Antarctica (Fig. 5q).

It is important to note that, we are not aiming at reducing the regression model bias by including more predictors,

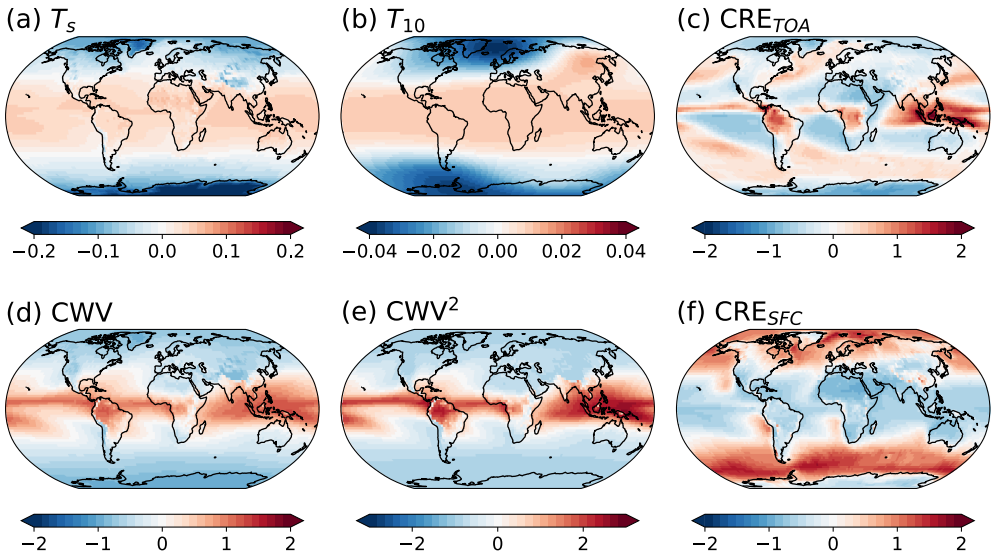

FIG. 4. The climatology of normalized predictors for multivariate regression models in equation 2 to 10: (a) surface temperature, T_s; (b) stratospheric temperature at 10hPa, T_{10}; (c) cloud radiative effect at the TOA, CRE_{TOA}; (d) column water vapor, CWV; (e) column water vapor squared, CWV^2; (f) cloud radiative effect at the surface, CRE_{SFC}. The sign of column water vapor and column water vapor square may differ because of the normalization.

which could lead to overfitting. Instead, we aim to understand what makes up the forcing variability from a broad, realistic view before diving deep into spectroscopy. Some persisting biases, like the underestimated surface forcing in deserts and TOA forcing along west coasts, can be improved by adding surface pressure and 2-meter water vapor pressure as predictors. Despite being simple in form, the regression model already reveals some questions worth further exploration. For example, if the strong T_s contribution to TOA forcing is understood as the blocked surface emission, how come it ends up negligible in the atmospheric forcing? Also, it is straightforward to expect that the TOA and surface forcing are mostly positive before conducting radiative transfer calculation, but why does additional CO_2 actually decrease the atmospheric forcing in high latitudes? These questions prompt a more detailed investigation into the spectral dimension of the forcing, as discussed in the next section.

5. Attributing the source of TOA forcing

a. Method

To further establish the relationship between geophysical variables and forcing variability, we examine the relationship of TOA forcing between the surface and atmosphere from spectroscopy via analyzing the results of RRTMG's bands. This method allows one to further link the forcing to the surface or atmospheric condition. It also bears on the two traditional views of radiative forcing, the broadband absorptivity change and emission layer displacement. A similar concept was discussed in Dufresne et al. (2020) for individual atmospheric states, and here we are offering an evaluation that covers the range of climate states across the globe.

To trace the source of radiative fluxes, we review the integrated non-scattering radiative transfer equation:

$$I(0) = I(\tau^*)\, e^{-\tau^*} + \int_0^{\tau^*} B(\tau)\, e^{-\tau}\, d\tau, \qquad (11)$$

where I is the monochromatic radiance, $B(\tau)$ is the thermal emission of the layer with optical depth τ associated with transmissivity $Tr = e^{-\tau}$. The optical depth is set downward positive, with zero at the TOA and τ^* at the surface. This equation states that the radiance is the summation of transmitted emission from the source and transmitted emission by layers in between. With instantaneous CO_2 doubling, the emission profile is unchanged in height coordinate: only $\tau(z)$ is perturbed. To draw a more intuitive connection between the radiance and atmospheric profile, equation (11) can be alternately expressed in height coordinates as,

$$I(\infty) = I(0)\, Tr^* + \int_0^{\infty} B(z)\, W(z)\, dz, \qquad (12)$$

where $Tr^* \equiv e^{-\tau^*}$ is the fraction of surface emission that is transmitted to the TOA, hereby named the total transmissivity. $W(z)$ is the weighting function, defined as the derivative of transmission function with height:

$$W(z) = \frac{dTr(z)}{dz} = e^{-\tau(z)}\, \frac{d\tau(z)}{dz}. \qquad (13)$$

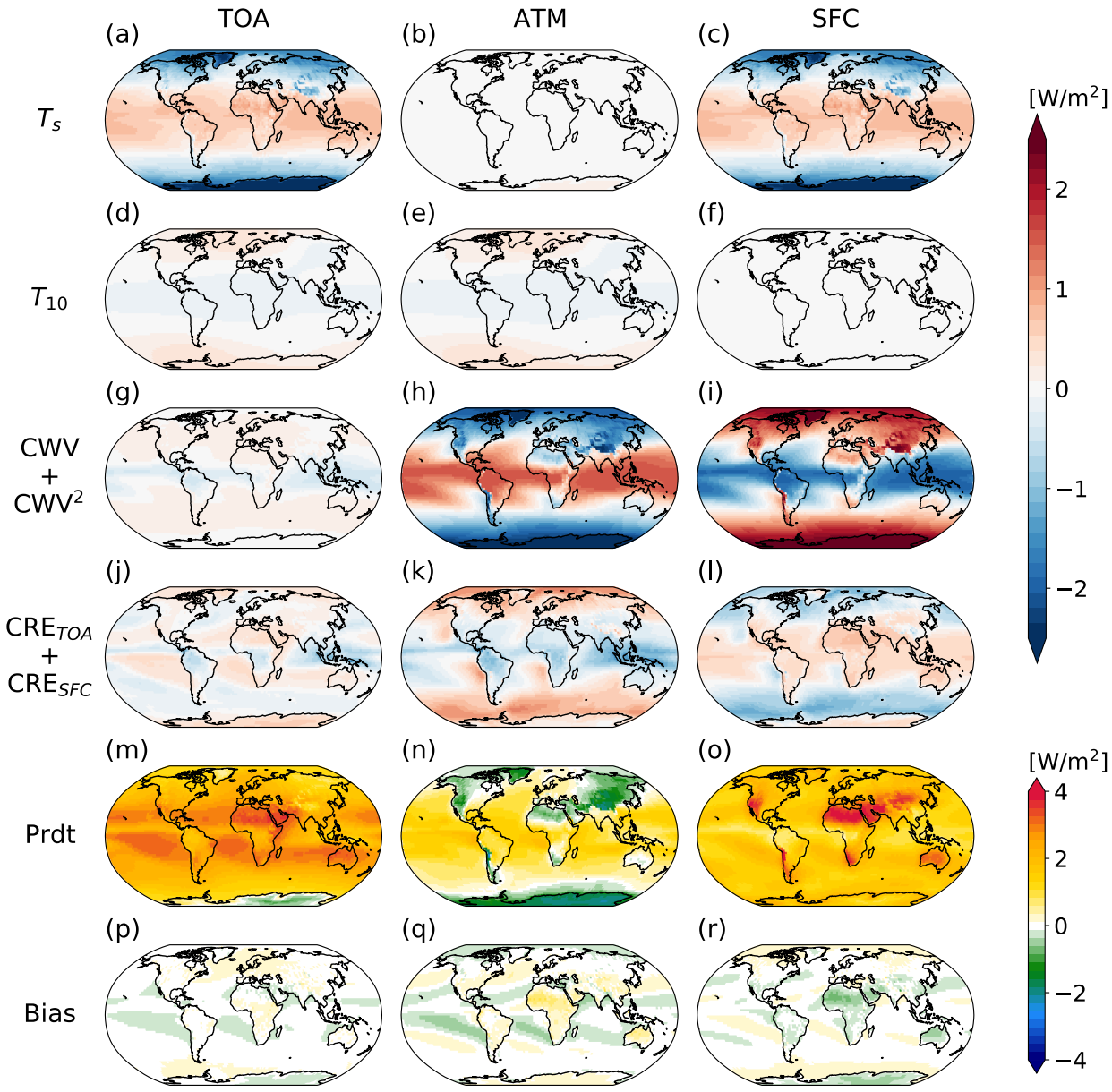

FIG. 5. From top to the fourth row: The partial contribution of multiyear mean forcing anomaly at the (left) TOA, (middle) atmosphere, and (right) surface by multiplying the regression coefficients in equation (2)- (10) with predictor anomalies. The predicted all-sky forcing (the sum of top four rows plus the multiyear global-mean forcing) and the bias are shown in bottom two rows.

A typical weighting function for upward flux exhibits a bell-shaped structure which maximizes at the altitude where $\tau = 1$, meaning that the majority of TOA flux comes out from a relatively narrow range of altitudes that is referred as the "emission layer". This allows one to define a corresponding emission temperature, but such emission temperature is highly varying spectrally as the equation (11) is only valid for monochromatic radiances. For instantaneous CO_2 doubling, the TOA forcing is reflected in the change of Tr^* and $W(z)$ structure, and the relative effects of Tr^* and $W(z)$ depend on the extent to which the local absorption is saturated. In a transparent, optically thin atmosphere ($Tr^* > e^{-1} \approx 0.37$), both Tr^* and $W(z)$ can change with additional CO_2. In contrast, for regions where the absorption is saturated ($Tr^* \approx 0$), there is no room for Tr^* to decrease and therefore the change of fluxes can only come from $W(z)$ variation. We will show in what follows that CWV is highly correlated to the broadband Tr^* in the current climate's atmosphere, helping to quan-

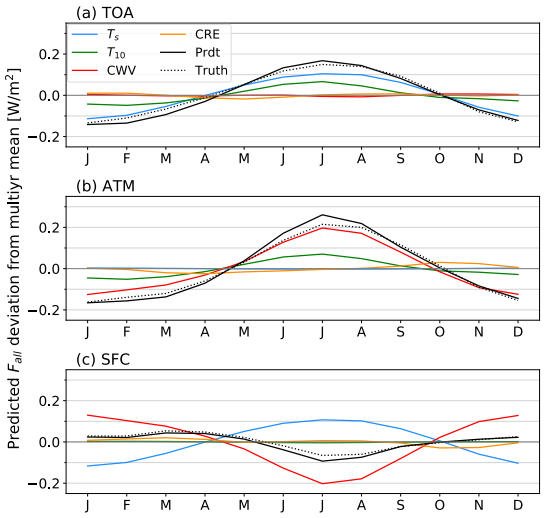

FIG. 6. The seasonality of global-mean forcing anomaly predicted by the multivariate regression model for the (a) TOA, (b) atmospheric, and (c) surface forcing. Each line identifies the partial contribution by (blue) surface temperature, T_s; (green) stratospheric temperature at 10hPa, T_{10}; (red) column water vapor, which includes the CWV and CWV^2 components, (orange) cloud radiative effect at the TOA or/with surface according to equation (8)- (10), and (black solid) the total prediction. The global-mean forcing calculated with RRTMG, the truth, is shown in the black dashed line.

tify the role of higher specific humidity on the saturation of radiative absorption.

An immediate benefit of identifying Tr^* and $W(z)$ contribution to the forcing is to untangle how the temperature structure comes into play. When Tr^* is large, the atmosphere is transparent. Additional CO_2 absorbs more radiance, increasing the absorptivity of the air. A weakly absorbing atmosphere can be approximated as an isothermal one, and the forcing depends on the amount of Tr^* change as well as temperature difference between the surface and atmospheric emission temperature (Dufresne et al. 2020). In contrast, in optically thick case, the CO_2 forcing depends on the difference between new and old emission temperature that is not directly related to the surface temperature. Instead, the lapse rate near the emission layer displacement would be key. With this context, Tr^* is not only a number describing the portion that the surface emission passes through the atmosphere, it also determines the extent that the TOA forcing is connected to the surface temperature.

Here, we use the optical depth in RRTMG to calculate Tr^* and combine it with the surface emission $I(0)$ to determine the transmitted surface emission that reaches the TOA [the first term in the right-hand side of equation (12)] and the change in TOA flux from atmospheric emission is treated as the the remainder [the second term in the right-hand side of equation (12)]. From the difference of equation (12) between two CO_2 concentrations, we can separate the forcing into two components. The first forcing term, associated with total transmissivity change (ΔTr^*) and surface emission, is named as the surface contribution:

$$F_{TOA\_from\_SFC} = -I(0) \cdot \Delta Tr^* \tag{14}$$

$$\Delta Tr^* \equiv Tr^*_{2\mathrm{xCO_2}} - Tr^*_{1\mathrm{xCO_2}}. \tag{15}$$

The negative sign on the right-hand side of equation (14) converts the forcing to downward positive, following the convention for radiative forcing. We call the rest of forcing, that coming from $W(z)$ change, the atmospheric contribution:

$$F_{TOA\_from\_ATM} = F_{TOA} - F_{TOA\_from\_SFC}. \tag{16}$$

We do not further decompose the $W(z)$ structure in detail. We only apply this decomposition method to the TOA forcing because $W(z)$ for the surface forcing is bottom heavy and the effective emission height is sufficiently close to the ground that meaningful analyses require very high vertical resolution near the surface.

For the sake of computation and storage capacity, the analyses in this section are based on the annual-mean atmosphere under clear-sky for the year 2010. As the major findings do not explicitly depend on absolute location but are more related to the geophysical variables of these local conditions, we expect the results are also applicable to shorter timescales. For simplicity, the bandwise calculations are binned into three groups according to the optical properties associated with CO_2: the center of CO_2 absorption band (630-700 cm^{-1}), wings (500-630 cm^{-1} and 700-820 cm^{-1}), and the atmospheric window (820 to 1180 cm^{-1}). The effective broadband results are weighted by the surface emission spectrum. The bands with weak CO_2 forcing changes (wavenumber smaller than 500 cm^{-1} or larger than 1180 cm^{-1}) constitute less than 3% of broadband forcing and are ignored here.

b. Results

Figure 7 shows the spatial pattern of total transmissivity and its change in the three grouped bands described above. The CO_2 band center is fully opaque, with zero Tr^* everywhere due to strong CO_2 absorption. In the wings, CO_2 absorption partly overlaps with the water vapor rotation band, particularly in 500-630 cm^{-1}. The Tr^* distribution then reflects CWV because water vapor is the most significant greenhouse gas, with lower Tr^* in wet regions and increased Tr^* in severely dry areas like Greenland, the Tibetan Plateau, the Andes, and the Antarctic. In the atmospheric window, the atmosphere is substantially less absorbing everywhere yet it still displays a pattern resembling the climatology of CWV.

The change of total transmissivity (ΔTr^*) with CO_2 doubling does not alter the global pattern of Tr^*, as ΔTr^* is

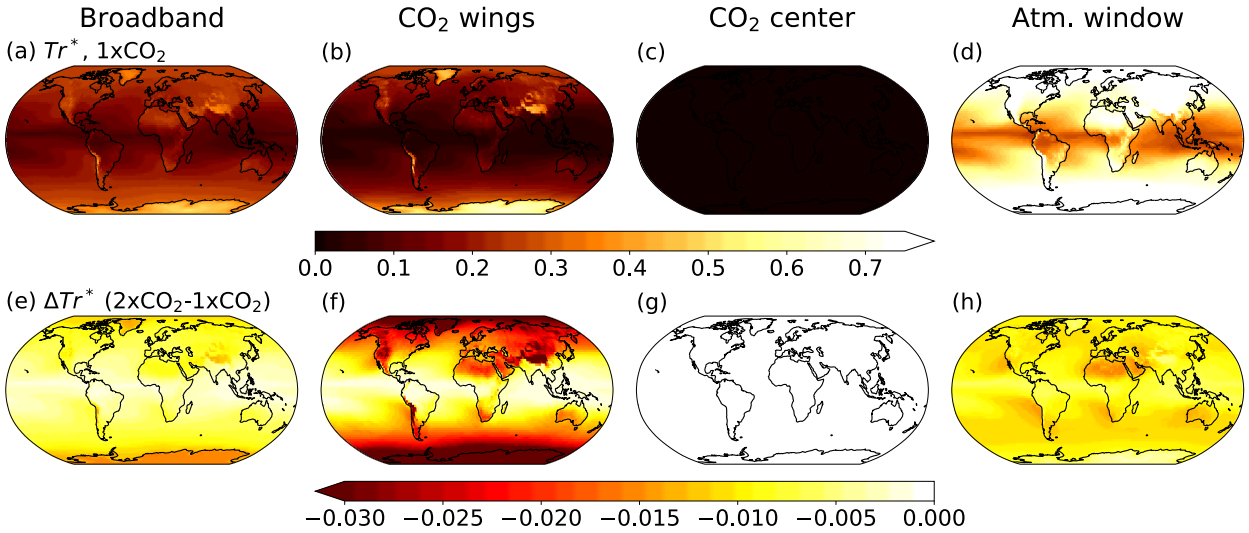

FIG. 7. (a-d) Total transmissivity (Tr^*) of the atmosphere and (e-h) total transmissivity change (ΔTr^*) with CO_2 doubling based on an annual-mean, cloudless atmosphere. As the absorptivity equals to $1-Tr^*$ in a non-scattering atmosphere, the absolute value of ΔTr^* is also the absorptivity change. In panel (g), all data equal to zero. CO_2 wings includes 500-630 and 700-820 cm^{-1} bands; CO_2 center refers to 630-700 cm^{-1}; atmospheric window contains the 820-980, 980-1080, and 1080-1180 cm^{-1} bands. The CO_2 wings, center, and atmospheric window do not add up to broadband (a and e) as some bands (wavenumber smaller than 500 cm^{-1} or larger than 1180 cm^{-1}) are omitted.

an order of magnitude smaller than Tr^* (Figs. 7e-h). The Tr^* in the CO_2 band center is unchanged by increased CO_2 as the absorption is already saturated with the control concentration. For the CO_2 wings, ΔTr^* exhibits a pattern that is the reverse to Tr^*, with more ΔTr^* decrease in the polar regions and deserts, where the column is relatively transparent. This pattern also underlies the water vapor masking effect—that the water vapor and CO_2 overlapping at an absorbing band prevents absorption by additional CO_2. Although considerably weaker, the masking effect is also seen in the atmospheric window.

Figure 8a-d compares Tr^*, ΔTr^*, and their connections with CWV in further detail. Aside from the CO_2 band center, it is apparent that the Tr^* increases in drier columns, accompanied with larger magnitude of ΔTr^*. Interestingly, ΔTr^* appears linearly related to Tr^*, except for the driest locations. The driest locations, where CWV is less than $\approx 10\,kg\,m^{-2}$, correspond to regions such as Antarctica, Greenland, and the Tibetan Plateau, where the terrain is elevated and the surface temperature is extremely low.

The pattern of surface and atmospheric contribution to the TOA forcing is shown in Figure 9. The forcing contribution from the surface stems from non-zero ΔTr^* in the CO_2 wings and atmospheric window (Figs. 9a,b,d). The water vapor masking effect is clear in the CO_2 wings, as the forcing is largely reduced in the tropics. Since no surface emission can penetrate the thick atmosphere in the CO_2 absorption band center, the surface does not contribute to the TOA forcing there in this band and all of the forcing comes from the atmosphere (Figs. 9c,g). The sign of surface contribution is non-negative everywhere, while the atmospheric contribution can be either positive or negative. In the CO_2 band center, the emission layer is located within the stratosphere, and when the emission layer is raised by extra CO_2, the negative lapse rate in the surrounding leads to an increase in longwave cooling and therefore the atmosphere itself negatively contributes to the forcing (Fig. 9g; Huang et al. 2016; Jeevanjee et al. 2021). Similar reasoning is also applicable to positive atmospheric contribution in CO_2 wings. The only difference is that the emission layer is moved inside the troposphere, and the positive lapse rate there means that the added CO_2 decreases the emission temperature (Fig. 9f).

A counter-intuitive feature is that the atmosphere can negatively contribute to the TOA forcing outside of CO_2 absorption band. This is seen in the high latitudes of CO_2 wings and everywhere in the window band (Figs. 9f,h). These regions are optically-thin (Figs. 7b,d) and are not expected to have an emission layer within the stratosphere, which would allow the negative stratospheric lapse rate argument to be invoked. Instead, in these weak absorbing regions with $Tr^* > e^{-1}$, $W(z)$ appears to have a bottom-heavy profile. As ΔTr^* is much smaller than Tr^*, the emission layer remains at the bottom of the column and does not shift with additional CO_2. The additional CO_2 reduces transmissivity (Tr^*), while absorptivity ($1-Tr^*$) increases. As a result, the emissivity is increased in accordance with Kirchhoff's Law of Radiation. With increased emissivity, there is more emission from the atmosphere to space. Although such a transparent atmosphere reduces the

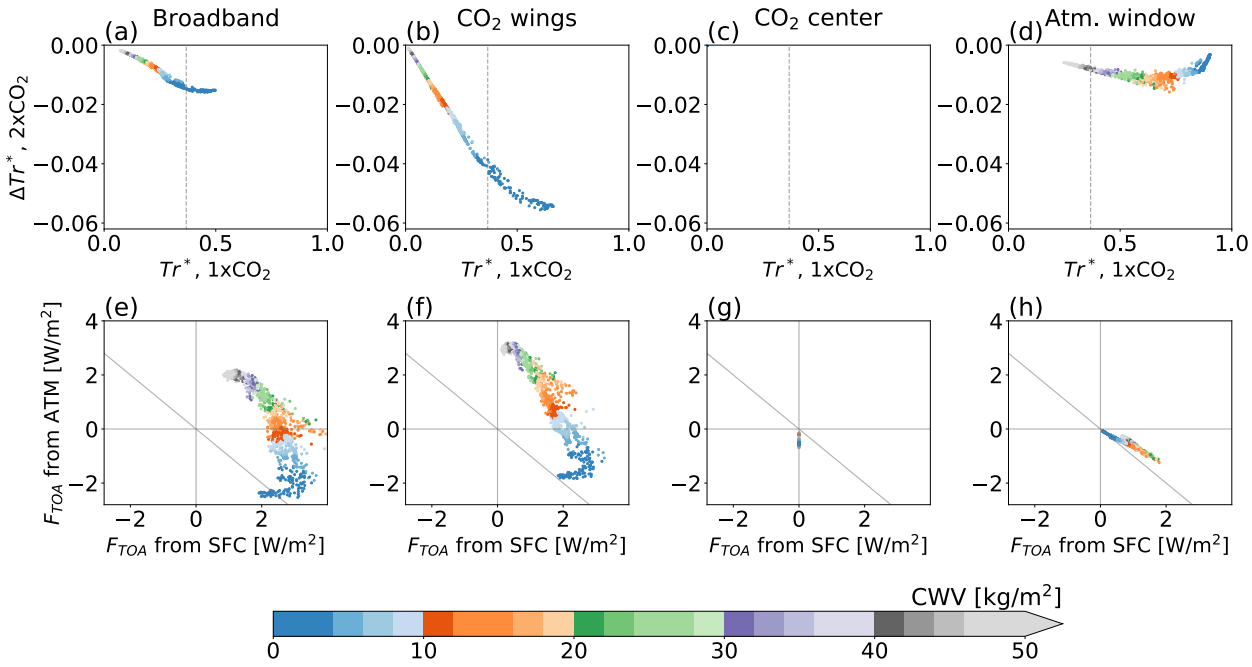

FIG. 8. (a-d) The change of total transmissivity (ΔTr^*) from CO_2 doubling versus total transmissivity (Tr^*) of the control CO_2. The gray dashed line denotes $Tr^* = e^{-1} \approx 0.37$. When $Tr^* < e^{-1}$, $W(z)$ is bell-shaped with an emission layer $\tau = 1$ within the atmosphere. Otherwise, $W(z)$ would be bottom-heavy with $Tr^* > e^{-1}$. The emission layer would be in the lowermost atmosphere but is not identical to traditionally defined $\tau = 1$ layer. (e-h) The TOA forcing originating from the atmosphere versus the TOA forcing originating from the surface, or, equivalently, the TOA forcing contributed by the emission layer change versus absorption change [equation (16) and (14), respectively]. The gray slanted line is $x + y = 0$ and the distance from this line equals the magnitude of TOA forcing. The dots are color-coded by column water vapor in kg m^{-2}. No data is shown in (c) because the absorption in CO_2 band center is fully saturated and therefore Tr^* and ΔTr^* both equal to zero. The grouping of bands is the same as Figure 7.

forcing, it does not override the surface contribution and the forcing in the particular band is still positive (Figs. 8f,h and Figs. 9j,l). As shown in Figure 8e-h, the bandwise TOA forcing is always positive in CO_2 wings and atmospheric window yet is very close to zero in the Antarctic, where CWV is less than 5 kg m^{-2}. Figure 8e-h also shows that the negative broadband TOA forcing over Antarctica results from relatively strong cooling in the CO_2 band center (Fig. 8g and Fig. 9k).

Figure 10 presents the relationship between the surface and atmospheric forcing and the decomposed TOA forcing components. The TOA forcing originating from the atmosphere matches the atmospheric forcing well, and similarly, the TOA forcing coming from the surface is very close to the surface forcing in most bands. The only inconsistency occurs in the CO_2 band center which is particularly opaque. The TOA and surface radiative fluxes are thus independent since the emission layer is very high for outgoing longwave at the TOA, while being very close to the surface for the downward surface flux.

By physically decomposing the source of TOA forcing based on spectroscopy, the choice of predictors in the regression models is justified and further reveals the intrinsic difference between the surface and atmospheric forcing. For the surface forcing, CWV explains large percentage of surface forcing pattern as it is highly correlated to ΔTr^* (Figs. 8a-d), but the surface temperature is still essential for satisfying surface forcing predictions since the surface emission can only be represented by T_s (Fig. 5c). In contrast, the atmospheric forcing can be qualitatively captured by CWV alone, as CWV greatly shapes the transmissivity pattern.

6. Conclusions and Discussion

In this study, we thoroughly investigated the instantaneous forcing of CO_2 doubling at the TOA, at the surface, and within the atmosphere. We demonstrated how the forcing patterns exhibit significant seasonal and geographical variability. The TOA forcing has clear meridional structure in the multiyear climatology, whereas the surface forcing is more variable zonally and is heavily influenced by humidity. Overall, the atmospheric forcing in the deep tropics is quite smooth, yet it exhibits a noticeable land-sea contrast with the opposite sign of forcing in the subtropics and midlatitudes. Over the subtropics and midlatitudes, the atmospheric forcing is generally negative over land, implying that increased CO_2 diminishes local longwave fluxes,

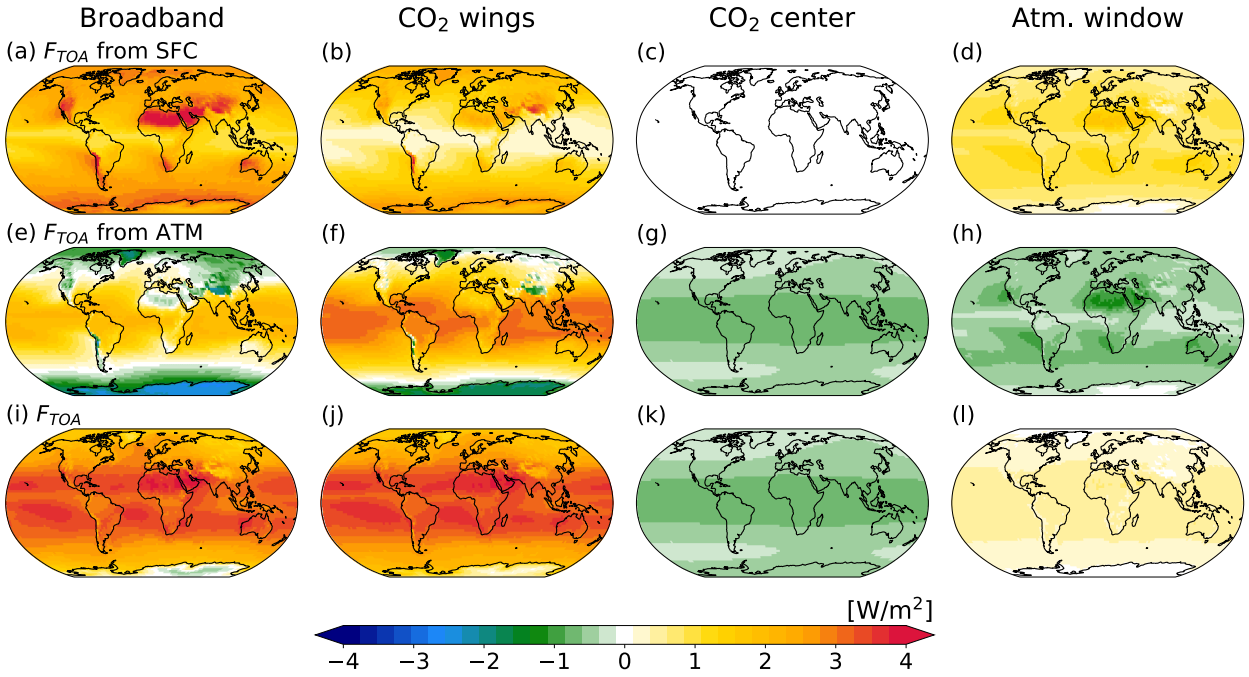

FIG. 9. Same as Figure 7 but for (a-d) the spatial pattern of TOA forcing originating from the surface [equation (14)], (e-h) TOA forcing originating from the atmosphere [equation (16)] and (i-l) the total TOA forcing in the bands (left to right columns) indicated by the titles. The first and second rows sum to the bottom row. All data in panel (c) is equal to zero.

which has not been highlighted in the past. However, the strong surface forcing may lead to rapid warming over land regions. In terms of temporal variation, the forcing is rather steady between years, but displays significant seasonality. The seasonality of global-mean surface forcing goes in the opposite direction to the global-mean TOA forcing. The TOA forcing maximizes in northern hemisphere summer, which is also the season with the minimum surface forcing. Therefore, the atmospheric forcing in boreal summer is about twice as strong as that in boreal winter, implying a non-negligible seasonality on the global-mean atmospheric energy budget.

Then, we used multivariate regression models, a convenient method to estimate the forcing pattern with the information of just surface temperature, stratospheric temperature, column water vapor, and cloud radiative effect. We show that the TOA forcing is mostly determined by the surface and stratospheric temperatures, with slight modification made by the cloud and water vapor masking effects. In contrast, water vapor explains the majority of the variation in the surface forcing; though one must also take surface temperature into account. Interestingly, we find that the surface temperature's contribution to the TOA and surface forcing essentially cancel out, and the surface temperature has a small magnitude contribution for the atmospheric forcing regression model. These models successfully capture the majority of the forcing inhomogeneity and seasonality, despite their simplicity.

Furthermore, there is a crucial role for water vapor plays in determining the forcing pattern, particularly for the atmospheric forcing. When the atmosphere is dry (absorption is unsaturated with high Tr^*), the transmissivity changes. Additional CO_2 prevents more surface emission from passing through the atmosphere and reduces outgoing longwave flux at the TOA, leading to positive forcing there. Meanwhile, as CO_2 concentration rises, it also increases emissivity and emits more longwave flux, which reduces TOA forcing and creates negative forcing for the atmosphere. In contrast, the absorptivity cannot increase in a moist air column where the greenhouse effect is saturated ($Tr^* \approx 0$). Instead, the emission layer is raised to a higher altitude, causing the emission temperature to vary, making the lapse rate between the original and perturbed emission layers an important aspect of the forcing. Although the sign of relevant lapse rate varies with spectral features, it is generally positive in terms of the broadband fluxes, resulting in greater TOA and positive atmospheric forcing in hot and humid regions. The sign variation of atmospheric forcing is therefore not coincidental, but highlights the distinct roles of water vapor in determining the forcing.

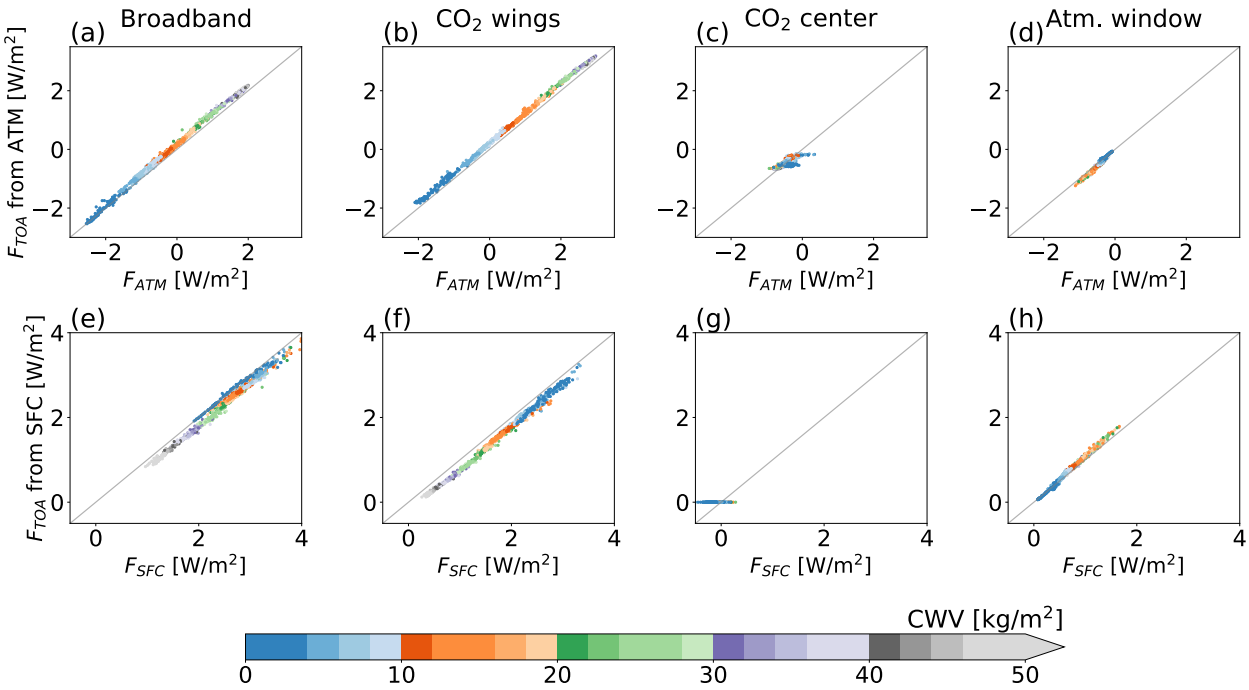

FIG. 10. The decomposed TOA forcing components versus forcing at the surface and the atmosphere. (a-d) TOA forcing originating from the surface (owing to total transmissivity change, ΔTr^*) versus the surface forcing and (e-h) TOA forcing originating from the atmosphere (due to emission layer displacement in saturated, moist columns and emissivity increase in cold, dry columns) versus atmospheric forcing. The dots are color-coded by column water vapor in kg m^{-2}, and the grouping of bands is the same as Figure 7.

Numerous intriguing aspects are revealed by these forcing assessments. In addition to the highly variable pattern itself, one interesting question is how the forcing at the TOA, surface, and the atmosphere work together to adapt in order to restore energy balance. For example, as shown in Figure 1, it is known that the amplified TOA forcing at subtropical subsiding region mitigates the meridional energy gradient that a thermal direct circulation needs to adjust, leading to an anomalous upward branch of circulation (Merlis 2015). Strong surface forcing may also cause the surface to warm up. The following negative atmospheric forcing, however, could lead to increased subsidence by localized radiative cooling. How much of the respective forcing may give rise to large-scale circulation changes as opposed to local rebalancing via column adjustments and land surface temperature change warrant future investigation.

Acknowledgments. We acknowledge the supports of the Natural Sciences and Engineering Research Council of Canada (RGPIN-2019-04511, RGPIN-2019-05225), the Fonds de Recherche Nature et Technologies of Quebec (2021-PR-283823), Compute Canada/Canada Foundation for Innovation computing allocation and a Canada Research Chair (TMM). YTC acknowledges the supports of Stephen & Anastasia Mysak Fellowship of McGill University.

Data availability statement. The ERA5 datasets can be accessed through the ECMWF website (https://cds.climate.copernicus.eu/). The RRTMG code can be downloaded at http://rtweb.aer.com/rrtm_frame.html. The forcing dataset and scripts for figures are available at https://doi.org/10.5281/zenodo.7076271.

References

Allen, M., and W. Ingram, 2002: Constraints on future changes in climate and the hydrologic cycle. *Nature*, **419**, 228–232.

Collins, W. D., and Coauthors, 2006: Radiative forcing by well-mixed greenhouse gases: Estimates from climate models in the Intergovernmental Panel on Climate Change (IPCC) Fourth Assessment Report (AR4). *Journal of Geophysical Research: Atmospheres*, **111 (D14)**, https://doi.org/https://doi.org/10.1029/2005JD006713.

Costa, S. M. S., and K. P. Shine, 2012: Outgoing longwave radiation due to directly transmitted surface emission. *J. Atmos. Sci.*, **69 (6)**, 1865–1870.

Dufresne, J.-L., V. Eymet, C. Crevoisier, and J.-Y. Grandpeix, 2020: Greenhouse effect: The relative contributions of emission height and total absorption. *J. Climate*, **33 (9)**, 3827–3844.

Feldl, N., and G. H. Roe, 2013: The nonlinear and nonlocal nature of climate feedbacks. *J. Climate*, **26**, 8289–8304.

Feldman, D. R., W. D. Collins, P. J. Gero, M. S. Torn, E. J. Mlawer, and T. R. Shippert, 2015: Observational determination of surface radiative forcing by CO_2 from 2000 to 2010. *Nature*, **519**, 339–343.

Flanner, M. G., X. Huang, X. Chen, and G. Krinner, 2018: Climate response to negative greenhouse gas radiative forcing in polar winter. *Geophys. Res. Lett.*, **45 (4)**, 1997–2004.

Freese, L. M., and T. W. Cronin, 2021: Antarctic radiative and temperature responses to a doubling of CO_2. *Geophys. Res. Lett.*, **48 (17)**, e2021GL093 676.

Huang, Y., and M. Bani Shahabadi, 2014: Why logarithmic? A note on the dependence of radiative forcing on gas concentration. *J. Geophys. Res. Atmospheres*, **119 (24)**, 13,683–13,689.

Huang, Y., X. Tan, and Y. Xia, 2016: Inhomogeneous radiative forcing of homogeneous greenhouse gases. *J. Geophys. Res.*, **121**, 2780–2789.

Huang, Y., Y. Xia, and X. Tan, 2017: On the pattern of CO_2 radiative forcing and poleward energy transport. *J. Geophys. Res.*, **122 (20)**, 10,578–10,593.

Iacono, M. J., J. S. Delamere, E. J. Mlawer, M. W. Shephard, S. A. Clough, and W. D. Collins, 2008: Radiative forcing by long-lived greenhouse gases: Calculations with the aer radiative transfer models. *Journal of Geophysical Research: Atmospheres*, **113 (D13)**, https://doi.org/https://doi.org/10.1029/2008JD009944.

Jeevanjee, N., and S. Fueglistaler, 2020: On the cooling-to-space approximation. *J. Atmos. Sci.*, **77 (2)**, 465 – 478, https://doi.org/10.1175/JAS-D-18-0352.1.

Jeevanjee, N., J. Seeley, D. Paynter, and S. Fueglistaler, 2021: An analytical model for spatially varying clear-sky CO_2 forcing. *Journal of Climate*, **34 (23)**, 9463 – 9480.

Merlis, T. M., 2015: Direct weakening of tropical circulations from masked CO_2 radiative forcing. *Proc. Nat. Acad. Sci.*, **112**, 13 167–13 171.

Pendergrass, A. G., and D. L. Hartmann, 2014: The atmospheric energy constraint on global-mean precipitation change. *J. Climate*, **27**, 757–768.

Pierrehumbert, R. T., 2010: *Principles of Planetary Climate*. Cambridge University Press, 688 pp.

Pincus, R., and Coauthors, 2020: Benchmark calculations of radiative forcing by greenhouse gases. *J. Geophys. Res.*, **125 (23)**, e2020JD033 483.

Romps, D. M., J. T. Seeley, and J. P. Edman, 2022: Why the forcing from carbon dioxide scales as the logarithm of its concentration. *J. of Climate*, **35 (13)**, 4027–4047.

Samset, B. H., and Coauthors, 2016: Fast and slow precipitation responses to individual climate forcers: A PDRMIP multimodel study. *Geophys. Res. Lett.*, **43 (6)**, 2782–2791.

Schmithüsen, H., J. Notholt, G. König-Langlo, P. Lemke, and T. Jung, 2015: How increasing CO_2 leads to an increased negative greenhouse effect in antarctica. *Geophys. Res. Lett.*, **42 (23)**, 10,422–10,428.

Seeley, J. T., N. J. Lutsko, and D. W. Keith, 2021: Designing a radiative antidote to CO_2. *Geophys. Res. Lett.*, **48 (1)**, e2020GL090 876.

Shakespeare, C. J., and M. L. Roderick, 2021: The clear-sky downwelling long-wave radiation at the surface in current and future climates. *Quarterly Journal of the Royal Meteorological Society*, **147 (741)**, 4251–4268.

Shaw, T. A., and Z. Tan, 2018: Testing latitudinally dependent explanations of the circulation response to increased CO_2 using aquaplanet models. *Geophys. Res. Lett.*, **45 (18)**, 9861–9869.

Zhang, M., and Y. Huang, 2014: Radiative forcing of quadrupling CO_2. *J. Climate*, **27**, 2496–2508.